

Spin pumping with coherent elastic waves

M. Weiler,¹ H. Huebl,¹ F. S. Goerg,¹ F. D. Czeschka,¹ R. Gross,^{1,2} and S.T.B. Goennenwein^{1,*}

¹Walther-Meißner-Institut, Bayerische Akademie der Wissenschaften, 85748 Garching, Germany

²Physik-Department, Technische Universität München, 85748 Garching, Germany

We show that the resonant coupling of phonons and magnons can be exploited to generate spin currents at room temperature. Surface acoustic wave (SAW) pulses with a frequency of 1.55 GHz and duration of 300 ns provide coherent elastic waves in a ferromagnetic thin film/normal metal (Co/Pt) bilayer. We use the inverse spin Hall voltage in the Pt as a measure for the spin current and record its evolution as a function of time and external magnetic field magnitude and orientation. Our experiments show that a spin current is generated in the exclusive presence of a resonant elastic excitation. This establishes acoustic spin pumping as a resonant analogue to the spin Seebeck effect.

The generation and detection of pure spin currents is vigorously investigated for the injection and transportation of spin information^{1–6}. Spin currents may be generated, e.g., via the spin Seebeck effect^{7–10}, or via spin pumping^{6,11–16}. In the latter approach, electromagnetic waves in the GHz regime, i.e., microwave *photons* are used to resonantly excite magnetization dynamics in a ferromagnet (FM) and thus drive a spin current into an adjacent normal metal (N). Here we show that the resonant absorption of elastic waves, i.e., microwave *phonons* in a FM/N bilayer can be used to acoustically drive a spin current. This establishes the spin current generation by a resonant phonon-magnon coupling and thus an interaction of lattice and spin degrees of freedom. In this sense, acoustic spin pumping can be seen as a resonant analogue of the spin Seebeck effect¹⁷. This resonant magnon-phonon coupling is a complementary approach to the non-resonant acoustic spin-current generation recently observed by Uchida *et al.*¹⁸ in a ferromagnetic insulator. In particular, we use a metallic ferromagnet and are able to tune the system in and out of acoustically driven ferromagnetic resonance via the application of an external magnetic field. As shown in the following, we find clear evidence for a resonant spin current generation. However, within the experimental sensitivity limit, we do not observe a spin current in the off-resonant condition. Our findings are thus in accordance with conventional, photon-FMR-driven, spin pumping experiments. The resonant phonon-spin current conversion discussed in this letter opens intriguing perspectives for applications in, e.g., microelectromechanical systems (MEMS), since elastic deformation can now be used for spin current generation. Thus, phonon-driven spin pumping is a pathway for the resonant generation of a spin current in the absence of a real, external electromagnetic driving field. Furthermore, phonon-driven spin pumping can be disentangled from microwave rectification effects induced by free space electromagnetic waves^{19–21}. Using time-resolved experiments, we are able to clearly distinguish such rectification effects from the inverse spin Hall voltage^{22,23} used to detect the acoustically driven spin pumping.

To demonstrate spin pumping via microwave phonons, we exploit phonon driven ferromagnetic resonance

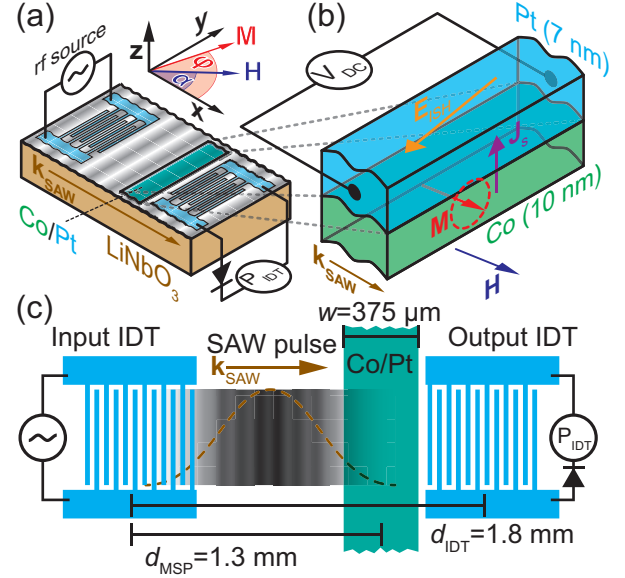


FIG. 1. (a) Schematic view of LiNbO₃/Co/Pt hybrid. An external static magnetic field H can be applied within the film plane at an angle α to the SAW propagation direction. (b) The SAW drives resonant magnetization M precession that emits a spin current J_s into the Pt. J_s is detected via the inverse spin Hall effect in the Pt thin film, i.e., as the voltage V_{DC} . (c) Sample geometry (not to scale). The SAW pulse first traverses the Co/Pt bilayer and then is detected at the output IDT.

(FMR)²⁴ in ferromagnet/normal metal bilayers. The acoustic FMR is excited by a surface acoustic wave (SAW) propagating in a cobalt/platinum (Co/Pt) thin film bilayer in the presence of an externally applied, static magnetic field. Via inverse magnetostriction²⁵, the SAW induces magnetization dynamics in the Co thin film which in turn generate a spin current at the Co/Pt interface. The sample is depicted schematically in Fig. 6(a). It consists of a Co (10 nm)/Pt (7 nm) bilayer deposited on LiNbO₃ between two Al (70 nm) interdigital transducers (IDTs)²⁶ with a periodicity of 20 μ m. For all results shown in this letter, the acoustic delay line shown in Fig. 6(a) is operated at its 9th harmonic frequency $\nu = 1.548$ GHz at room temperature. A SAW

is launched at the input IDT and induces a time varying pure lattice strain $\varepsilon(t) = \varepsilon \cos(2\pi\nu t)$ along x with amplitude ε into the ferromagnet²⁷. Via magnetoelastic coupling, $\varepsilon(t)$ excites magnetization \mathbf{M} precession as depicted schematically in Fig. 6(b). The magnetization precession can relax via the emission of a spin current \mathbf{J}_s into the normal metal (Pt)¹². We detect \mathbf{J}_s along z via the inverse spin Hall effect²², which results in an electric field $\mathbf{E}_{\text{ISH}} \propto \mathbf{M} \times \mathbf{J}_s$. More precisely, we measure $V_{\text{DC}} \propto \mathbf{E}_{\text{ISH}} \cdot \mathbf{y}$ (cf. Fig. 6(b)). The input IDT generates not only a SAW but also an electromagnetic wave (EMW) upon the application of a rf voltage. Thus, the aforementioned microwave rectification effects can contribute significantly to V_{DC} . However, since the velocity of the SAW (the speed of sound) is about five orders of magnitude slower than that of the EMW (the speed of light), a time resolved study of V_{DC} and the transmitted SAW power P_{IDT} allows for a separation of SAW and EMW driven effects. We thus apply SAW pulses as depicted in Fig. 6(c) and study the time dependent evolution of V_{DC} and P_{IDT} using a two channel oscilloscope. For the generation of the SAW pulses we apply +30 dBm rf pulses with $\nu = 1.548$ GHz, a pulse width $t_w = 310$ ns and a pulse period $t_r = 57.3$ μ s to the input IDT. By studying $P_{\text{IDT}}(t)$ and $V_{\text{DC}}(t)$ for various external magnetic field \mathbf{H} orientations and magnitudes we can unambiguously identify phonon driven spin-pumping as shown in the following.

We first turn to the separation of contributions to P_{IDT} and V_{DC} due to the SAW and the EMW. In Fig. 2(a) we show the transmitted rf power P_{IDT} as a function of time t for application of \mathbf{H} at $\alpha = 10^\circ$. As the SAW has a velocity of 3440 m/s and the sample features a center to center IDT spacing of 1.8 mm, the SAW transit time is $t_t = 0.52$ μ s. In contrast, the EMW propagates with the speed of light and is thus expected to appear almost instantaneously with the microwave pulse at $t \approx 0$. Indeed, in the $P_{\text{IDT}}(t)$ trace shown in Fig. 2(a), two signals are observed, the first of which begins at $t \approx 0$ and is attributed to the EMW. The rectangular shape and duration mimics the applied microwave pulse. At $t_{\text{SAW}} = 0.7$ μ s a Gaussian pulse of smaller magnitude is recorded. This pulse is due to the SAW reaching the output transducer. The separation of EMW and SAW pulses allows us to distinguish between photon and phonon driven contributions to $P_{\text{IDT}}(t)$. We now turn to the external magnetic field dependence of P_{IDT} shown in Fig. 2(b). Here we plot $\Delta P_{\text{IDT}} = P_{\text{IDT}}(\mu_0 H) - P_{\text{IDT}}(\mu_0 H_{\text{ref}})$. We use $\mu_0 H_{\text{ref}} = 30$ mT as reference magnetic field and investigate data obtained at the FMR magnetic field $\mu_0 H_{\text{res}} = \pm 4$ mT (dashed and dotted line, respectively). For both values of H , one observes a pronounced dip in ΔP_{IDT} at t_{SAW} . This SAW attenuation is attributed to acoustically driven FMR, which results in a damping of the SAW as detailed in Ref.²⁴. We now turn to the simultaneously recorded voltage $V_{\text{DC}}(t)$ in the Co/Pt bilayer. Since the latter is positioned at a distance of $d_{\text{MSP}} = 1.3$ mm from the input IDT, the SAW pulse is

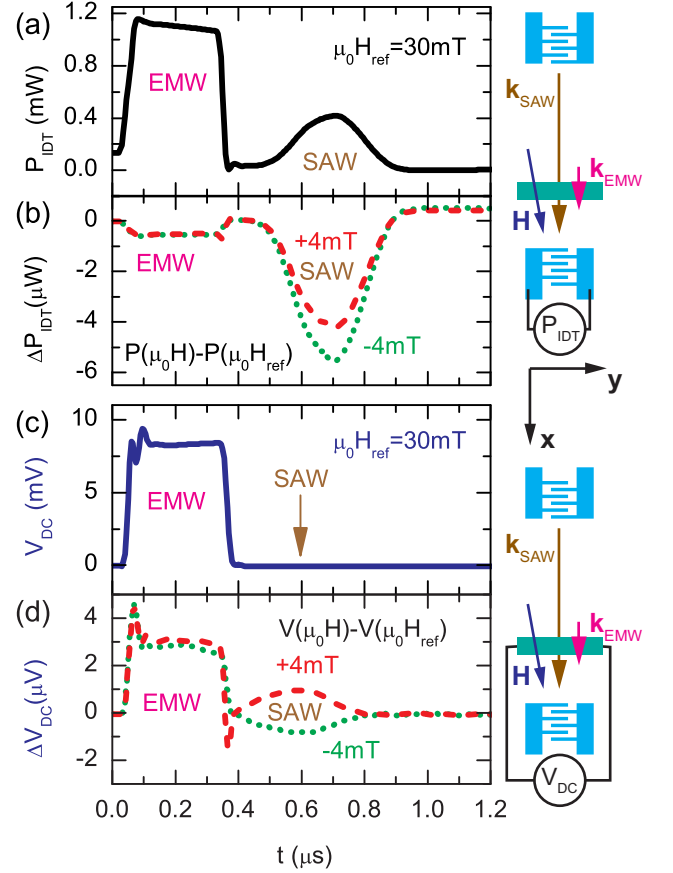


FIG. 2. Time resolved spectroscopy with \mathbf{H} applied at $\alpha = 10^\circ$. (a) P_{IDT} as a function of time with $\mu_0 H_{\text{ref}} = 30$ mT, showing the detection of the electromagnetic wave (EMW, 0.2 μ s) and the surface acoustic wave (SAW, 0.7 μ s) pulses at the output IDT. (b) $\Delta P_{\text{IDT}}(t) = P_{\text{IDT}}(t, \mu_0 H) - P_{\text{IDT}}(t, \mu_0 H_{\text{ref}})$. $\Delta P_{\text{IDT}}(0.7 \mu\text{s}) < 0$ shows that the SAW is damped for $\mu_0 H_{\text{res}} = \pm 4$ mT, indicating acoustically driven FMR. (c) V_{DC} as a function of time at $\mu_0 H_{\text{ref}} = 30$ mT. The EMW is rectified at the bilayer. (d) $\Delta V_{\text{DC}}(t) = V_{\text{DC}}(t, \mu_0 H) - V_{\text{DC}}(t, \mu_0 H_{\text{ref}})$. The change of sign of $\Delta V_{\text{DC}}(0.6 \mu\text{s})$ with reversal of \mathbf{H} direction is a signature of acoustic spin pumping.

expected to reach the bilayer 0.1 μ s before it is detected at the output IDT. This yields a maximum SAW amplitude at the bilayer at $t_{\text{MSP}} = 0.6$ μ s, while the EMW is again expected at $t \approx 0$. For $\mu_0 H_{\text{ref}} = 30$ mT we observe $V_{\text{DC}}(t)$ shown in Fig. 2(c), dominated by EMW driven effects as evident from its time dependence and shape. In particular, no signal is observed at t_{MSP} . This is not surprising, since no acoustic FMR and thus no spin current is excited for these parameters. In contrast, the FMR condition is fulfilled at $\mu_0 H_{\text{res}} = \pm 4$ mT. In Fig. 2(d) we plot $\Delta V_{\text{DC}} = V_{\text{DC}}(\mu_0 H) - V_{\text{DC}}(\mu_0 H_{\text{ref}})$ for $\mu_0 H = \pm 4$ mT (dashed and dotted line, respectively). Here, a clear feature can be observed at t_{MSP} . The sign reversal of $\Delta V_{\text{DC}}(t_{\text{MSP}})$ with respect to \mathbf{H} direction thereby is a necessary condition for the detection of

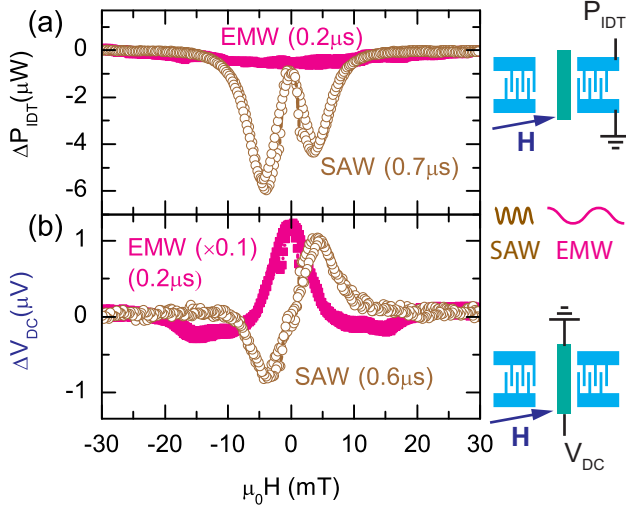


FIG. 3. (a) ΔP_{IDT} for the detection of the SAW (open symbols) and the EMW (solid symbols) pulse at the output IDT as a function of external magnetic field magnitude for \mathbf{H} applied at $\alpha = 10^\circ$. (b) ΔV_{DC} for the detection of the SAW (open symbols) and the EMW (solid symbols) pulse at the bilayer. The characteristic fingerprint for acoustic spin pumping is the antisymmetric behavior of ΔV_{DC} with respect to \mathbf{H} orientation.

a spin current via the inverse spin Hall effect¹⁵. In contrast, the EMW causes a field-symmetric contribution to ΔV_{DC} , which means that no EMW driven spin-pumping is observed.

The contributions to ΔP_{IDT} and ΔV_{DC} due to the SAW and EMW are now investigated as a function of H . We hereby take advantage of the separation of the SAW and EMW in the time domain and attribute $\Delta P_{\text{IDT}}(0.2 \mu\text{s})$ and $\Delta V_{\text{DC}}(0.2 \mu\text{s})$ to the interaction of the bilayer with the EMW and $\Delta P_{\text{IDT}}(0.7 \mu\text{s})$ and $\Delta V_{\text{DC}}(0.6 \mu\text{s})$ to the interaction of SAW and bilayer. Figure 3(a) shows $\Delta P_{\text{IDT}}(\mu_0 H)$ for both elastic and electromagnetic interaction. We find a very weak magnetic field dependence of the transmission of the EMW (solid symbols) which shows no indication for FMR driven by the EMW. We however observe a distinct resonant absorption of the SAW (open symbols) which we attribute to acoustically driven FMR²⁴. Turning to ΔV_{DC} shown in Fig. 3(b), we in contrast observe a sizeable magnetic field dependence of the EMW transmission at $t = 0.2 \mu\text{s}$ (solid symbols) attributed to microwave rectification effects²⁰. The signal shape however is distinctly different from that expected for the spin pumping effect, in particular no reversal of the sign of ΔV_{DC} with reversal of \mathbf{H} direction is observed. A detailed investigation of the origin and evolution of ΔV_{DC} due to EMW rectification is beyond the scope of this work. We refer to Refs.^{28,29}. At $t_{\text{MSP}} = 0.6 \mu\text{s}$ (open symbols) however, only the SAW pulse is present. Here, ΔV_{DC} shows a magnetic field dependence characteristic for spin pumping, in particular featuring a sign reversal with reversal

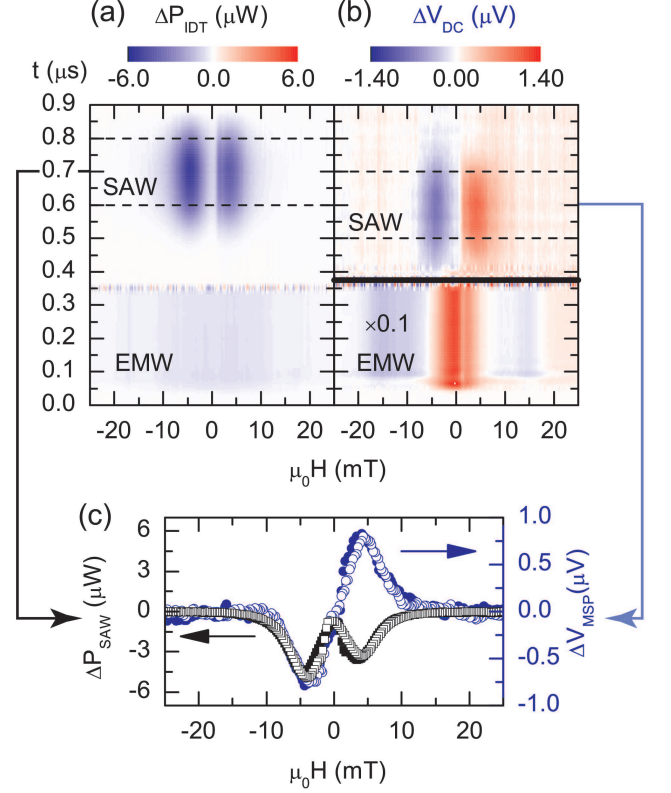


FIG. 4. (a) ΔP_{IDT} as a function of t and $\mu_0 H$ for \mathbf{H} applied at $\alpha = 10^\circ$. (b) $\Delta V_{\text{DC}}(t, \mu_0 H)$ shows EMW rectification (lower part, scaled by 0.1) while the SAW acoustically pumps a spin current which is detected via the inverse spin Hall effect (upper part). (c) We average ΔP_{IDT} and ΔV_{DC} data for the timespan indicated by the dashed lines in (a) and (b), respectively. These data correspond to all elastic excitation of FMR (ΔP_{SAW} , left scale) and a spin current (ΔV_{MSP} , right scale).

of \mathbf{H} direction and extrema at the FMR H field. We furthermore checked whether rf currents induced by the SAW E-Field into the Co/Pt could cause $\Delta V_{\text{DC}}(0.6 \mu\text{s})$. To this end, we deliberately applied such rf currents with $\nu = 1.548 \text{ GHz}$ to the bilayer³⁰, which resulted in a dc photovoltage V_{pv} attributed to rectification effects^{28,29,31} and spin-torque FMR³². As detailed in the supplementary information³⁰, the magnetic field dependence of V_{pv} is distinctly different to that of $\Delta V_{\text{DC}}(0.6 \mu\text{s})$. We thus attribute $\Delta V_{\text{DC}}(0.6 \mu\text{s})$ solely to elastically driven spin pumping.

To show the crucial separation of EMW and SAW driven contributions ($\Delta V_{\text{DC}}(\text{EMW}) \gg \Delta V_{\text{DC}}(\text{SAW})$) in a more complete fashion, we plot ΔP_{IDT} and ΔV_{DC} as a function of t and $\mu_0 H$ in Fig. 4(a) and (b), respectively (only magnetic field up-sweep shown). EMW rectification is observed for $t < 0.375 \mu\text{s}$ yielding a field-symmetric contribution to ΔV_{DC} . For the times corresponding to the presence of the SAW pulse, both ΔP_{IDT} and ΔV_{DC} are finite only for a narrow range around the FMR magnetic field $\mu_0 H_{\text{res}} = \pm 4 \text{ mT}$. One can observe

that ΔP_{IDT} is retarded by about $0.1 \mu\text{s}$ with respect to ΔV_{DC} (indicated by the dashed lines), in accordance to the propagation of the SAW along the delay line. For the investigation of phonon-driven spin pumping with good signal to noise ratio, we average ΔP_{IDT} and ΔV_{DC} for the time range indicated by the dashed lines. This yields the phonon-driven ΔP_{SAW} and ΔV_{MSP} , respectively. ΔP_{SAW} and ΔV_{MSP} are plotted in Fig. 4(c) as a function of H (solid symbols: H upswEEP, open symbols: H downswEEP). While a field symmetric absorption of rf power is observed for ΔP_{SAW} as expected for acoustically driven FMR²⁴, ΔV_{MSP} shows the antisymmetric behavior with respect to H orientation reversal characteristic of spin pumping. Furthermore, the resonance field and linewidth of ΔP_{SAW} and ΔV_{MSP} coincide. Outside of acoustically driven FMR (i.e. $\mu_0|H| > 10 \text{ mT}$), the SAW and thus phonons are still present in the ferromagnetic thin film. However, within the resolution of our experiment, $\Delta V_{\text{MSP}} = 0$ in this off-resonant condition.

Using the scaling law derived in Ref.¹⁵, we can calculate the resonant M precession cone angle Θ_{res} as:

$$\sin^2 \Theta_{\text{res}} = \frac{\Delta V_{\text{MSP}}}{e\nu PRwCg_{\uparrow\downarrow}} \quad (1)$$

with the elementary charge e , the ellipticity $P = 0.11$ calculated according to Ref.²¹, the resistance $R = 37 \Omega$ ³³ and width $w = 375 \mu\text{m}$ of the Co/Pt bilayer, the constant $C = 4.37 \times 10^{-11} \text{ m}^{15}$ and the spin mixing conductance of Co/Pt $g_{\uparrow\downarrow} = 6 \times 10^{19} / \text{m}^{215}$. With $\nu = 1.548 \text{ GHz}$ and $\Delta V_{\text{MSP}} = 0.8 \mu\text{V}$ from Fig. 4(c), Eq. (1) yields $\Theta_{\text{res}} = 1.6^\circ$, comparing well to values found for photon driven FMR in Co¹⁵. Out of resonance $\Delta V_{\text{MSP}} < 0.1 \mu\text{V}$ and hence the M precession cone angle is $\theta < 0.6^\circ$ assuming identical P . Using $\Theta_{\text{res}} = 1.6^\circ$, the strain caused by the SAW corresponds to a rf virtual driving field of $\mu_0 h_{\text{ME}} = \frac{1}{2} \mu_0 \Delta H \Theta_{\text{res}} = 73 \mu\text{T}$ with $\mu_0 \Delta H = 5.25 \text{ mT}$ extracted from Fig. 4(c) as the FWHM of ΔV_{MSP} at resonance. Note that this linewidth is just an estimate since the lineshape of acoustic FMR can deviate from a simple Lorentzian due to the particular properties of the magnetoelastic driving field^{24,30}. For acoustically driven FMR, h_{ME} is determined by the magnetic free energy density of the ferromagnetic Co film by²⁴

$$\mu_0 h_{\text{ME}} = 2 \frac{B_1}{M_s} \varepsilon \cos \varphi_0 \sin \varphi_0, \quad (2)$$

where $B_1 = 18 \text{ MJ/m}^{334}$ is the magnetoelastic coupling constant of Co, $M_s = 1.17 \times 10^6 \text{ A/m}^{35}$ the saturation magnetization and $\varphi_0 = 30^\circ$ the equilibrium orientation of M for H applied at $\alpha = 10^\circ$ calculated using the free energy approach detailed in Ref.²⁴. Equation (2) yields a strain $\varepsilon \approx 5.7 \times 10^{-6}$ in the ferromagnet due to the SAW pulse. In an independent experiment, we determined the SAW acoustic power $P_{\text{acoustic}} = 1 \text{ mW}$ by vector network analysis on the input IDT, resulting in a pure strain $\varepsilon = 9.8 \times 10^{-6}$ along x ³⁰. Thus, according to this order of magnitude estimation, the calculated SAW

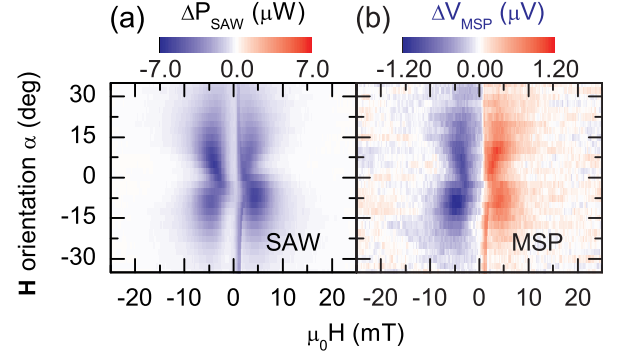


FIG. 5. (a) ΔP_{SAW} and (b) ΔV_{MSP} as a function of H orientation and magnitude for magnetic field upswEEP. The observed angular dependency is characteristic for acoustically driven FMR. The features around 2 mT are due to M reversal.

strain is large enough to account for ΔV_{MSP} by elastic spin pumping.

The characteristic fingerprint of acoustically driven FMR is its dependence on the orientation α of the externally applied magnetic field²⁴. Therefore, we recorded $\Delta P_{\text{IDT}}(t)$ and $\Delta V_{\text{DC}}(t)$ for $-35^\circ \leq \alpha \leq +35^\circ$ (Fig. 5). Fig. 5(a) shows the butterfly angular dependency of ΔP_{SAW} characteristic for acoustically driven FMR. In Fig. 5(b), we observe a finite ΔV_{MSP} only for values of α and H where the acoustically driven FMR condition is met, providing further evidence for phonon-driven spin pumping.

In conclusion, we have shown that a spin current can be generated by microwave phonons via rf magnetoelastic interaction in a Co/Pt thin film bilayer. By recording both, the generated inverse spin Hall voltage proportional to the spin current, and the SAW transmission as a function of time for various configurations of the externally applied magnetic field, we are able to discern between effects caused by photonic and phononic excitations. We find that a spin current is generated in the exclusive presence of an acoustic excitation of the Co thin film. This should enable the implementation of, e.g., microelectromechanical systems (MEMS) with the possibility to elastically generate spin current for future spintronic data processing applications. From a fundamental physics point of view our results are an important step towards the study of the interconversion of phononic and spin degrees of freedom.

Financial support from the DFG via GO 944/4-1, SPP 1538 and the German Excellence Initiative via the Nanosystems Initiative Munich (NIM) is gratefully acknowledged.

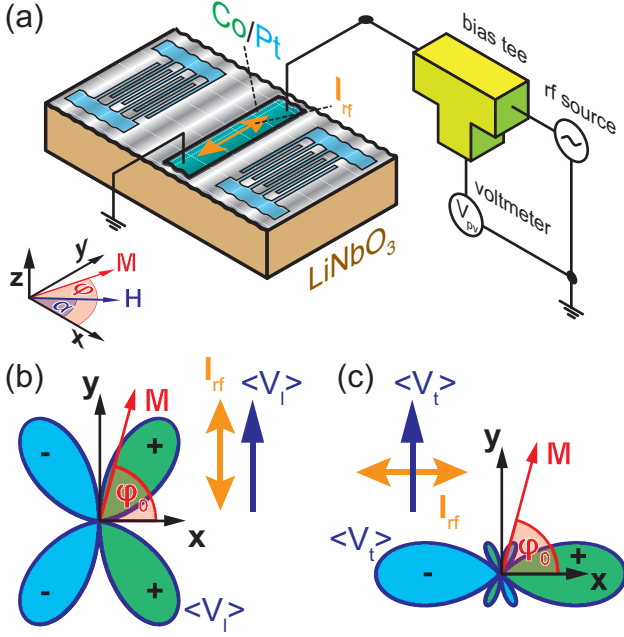


FIG. 6. (a) Schematic experimental configuration for the determination of the photovoltage V_{pv} . (b) For $\mathbf{I}_{rf} \parallel \mathbf{y}$ a longitudinal rectification voltage $\langle V_l \rangle$ is expected. $\langle V_l \rangle$ shows a characteristic dependence on the equilibrium \mathbf{M} orientation φ_0 similar to the one of V_{MSP} described in the main text. (c) For $\mathbf{I}_{rf} \parallel \mathbf{x}$, a transversal voltage $\langle V_t \rangle$ is expected along \mathbf{y} . $\langle V_t \rangle$ shows a dependence on φ_0 which is distinctly different than that of V_{MSP} .

Appendix A: DC voltage due to spin rectification and spin-torque effects

Surface acoustic waves (SAWs) travelling in piezoelectric substrates such as LiNbO_3 are accompanied by an electric potential³⁶ in addition to the mechanical displacement. The surface electrical potential of a SAW can be electrically shorted by a conductive thin film which results in a radio frequency (rf) current in the film. In our elastic spin pumping experiments (see main text), such SAW-induced rf currents in the conductive Co/Pt bilayer may give rise to dc voltages due to various mechanisms that result in resonant as well as non-resonant downmixing of the rf current^{28,29,31,32}. These rectification voltages may superimpose with the inverse spin Hall effect voltage V_{MSP} used to probe the acoustically driven spin current. To check whether such effects need to be considered in the interpretation of our V_{MSP} data, we *intentionally* exposed the Co/Pt bilayer to rf electrical currents and recorded the resulting dc voltages. To this end, the sample introduced in the main text was used. The Co/Pt bilayer was connected to a bias tee as schematically shown in Fig. 6(a) to enable the detection of dc voltages caused by the rf current applied along the \mathbf{y} axis by means of a microwave source (Rohde & Schwarz SMB100A) which was operated in continuous wave mode. A Keithley K2182

Nanovoltmeter was used to record the dc photovoltage V_{pv} .

Following the basic idea detailed in Ref.³², a rf current $\mathbf{I}_{rf}(t) = I_{rf,0} \cos(\omega t) \cdot \hat{\mathbf{e}}$ along direction $\hat{\mathbf{e}}$ in the Pt causes an Oersted field $\mathbf{h}_1(t) \perp \mathbf{I}_{rf}(t)$ in the Co thin film. The Oersted field induces magnetization \mathbf{M} precession if the condition for ferromagnetic resonance is met. This causes an oscillation of the bilayer resistance due to the anisotropic magnetoresistance (AMR)^{37,38}. Mixing of this resistance with the rf current yields a dc voltage. The voltage may be caused by an oscillation of the longitudinal or the transversal (planar Hall) resistance. As we only measure the voltage drop along \mathbf{y} we need to consider the longitudinal resistance for $\mathbf{I}_{rf} \parallel \mathbf{y}$ and the transversal resistance for $\mathbf{I}_{rf} \parallel \mathbf{x}$.

For $\mathbf{I}_{rf} \parallel \mathbf{y}$, a voltage drop along \mathbf{y} will be due to the longitudinal resistance

$$R_l(t) = R_{\perp} + \Delta R \sin^2 \varphi(t), \quad (\text{A1})$$

where $\varphi(t)$ is the angle enclosed between \mathbf{M} and \mathbf{x} , $\Delta R = R_{\parallel} - R_{\perp}$ and $\Delta R/R \approx 2\%$ in Co³⁷. We define $\varphi(t) = \varphi_0 + \Theta(t)$ with the equilibrium \mathbf{M} orientation φ_0 and the dynamic small angle \mathbf{M} precession $\Theta(t)$ around φ_0 . To first order in Θ we get

$$R_l(t) = R_{\perp} + \Delta R [\sin^2 \varphi_0 + 2 \cos \varphi_0 \sin \varphi_0 \Theta(t)].$$

We approximate $\Theta(t) = \cos(\omega t + \eta) \sin(\varphi_0) \Theta_{res}$ for the magnetization precession, where the factor $\sin(\varphi_0)$ accounts for the fact that only the component of \mathbf{h}_1 perpendicular to \mathbf{M} can drive the precession and η is the phase between driving field and \mathbf{M} precession. We thus find the time averaged longitudinal voltage

$$\begin{aligned} \langle V_l \rangle &= \langle R_l(t) I_{rf}(t) \rangle = V_{pv} \\ &= \Delta R \Theta_{res} \cos \eta I_{rf,0} \sin^2 \varphi_0 \cos \varphi_0, \end{aligned} \quad (\text{A2})$$

in accordance with the angular dependence of the mixing voltage defined in Eq. (2) in Ref.³². The normalized magnitude of $\langle V_l \rangle$ is plotted in the polar plot in Fig. 6(b) for $\eta = 0^\circ$. Thereby, the sign of $\langle V_l \rangle$ is indicated by the shading. $\langle V_l \rangle$ bears a similar symmetry as observed in V_{MSP} (see Fig. 5(b) in the main text). Thus, dc effects due to a rf current along \mathbf{y} need to be taken into account for the analysis of our elastic spin pumping data. This point will be addressed in more detail in Section C.

We now turn to a voltage drop along \mathbf{y} induced by $\mathbf{I}_{rf} \parallel \mathbf{x}$. This transversal voltage is caused by the transversal resistance

$$R_t(t) = \frac{\Delta R}{2} \sin[2\varphi(t)]. \quad (\text{A3})$$

Following the same line of argument as for $R_l(t)$, but with $\Theta(t) = \cos(\omega t + \eta) \cos(\varphi_0) \Theta_{res}$ we find

$$\langle V_t \rangle = \frac{1}{2} \Delta R \Theta_{res} \cos \eta I_{rf,0} \cos(2\varphi_0) \cos \varphi_0, \quad (\text{A4})$$

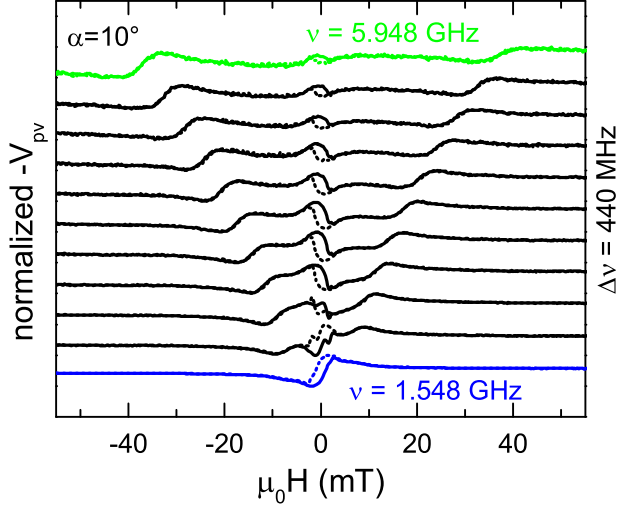


FIG. 7. Normalized and offset $-V_{pv}$ as a function of the external magnetic field $\mu_0 H$ upswEEP (solid) and downswEEP (dotted) for frequencies $1.548 \text{ GHz} \leq \nu \leq 5.948 \text{ GHz}$. Frequency was increased from bottom to top by $\Delta\nu = 440 \text{ MHz}$. For each frequency, at the ferromagnetic resonance frequency a dominantly antisymmetric line is recorded. In addition, non-resonant and hysteretic spin rectification near zero external magnetic field is observed.

which is depicted in the polar plot in Fig. 6(c) for $\eta = 0^\circ$. The magnitude of this dc voltage is maximal for $\varphi_0 = 0^\circ$ and its symmetry is more complex than that observed in V_{MSP} (see Fig. 5(b) in the main text).

Thus, we can exclude rectification voltages due to rf currents along \mathbf{x} as a contribution to V_{MSP} due to their dependence on the *orientation* of the external magnetic field \mathbf{H} which is significantly different to that observed in V_{MSP} (see main text). This leaves rectification voltages due to $\mathbf{I}_{rf} \parallel \mathbf{y}$. In the following, we experimentally demonstrate that latter bear a distinctly difference dependence on the *magnitude* of \mathbf{H} which results in different lineshapes of V_{MSP} and V_{pv} .

Appendix B: Experimental determination of dc photovoltage

We performed an rf impedance measurement by vector network analysis on the bilayer from which we obtained the rf current density $i_{rf} = 1.6 \times 10^9 \text{ A/m}^2$ in the Co/Pt bilayer at a power level $P = +17 \text{ dBm}$ and $\nu = 1.548 \text{ GHz}$. To demonstrate the rectification of rf currents, we determined V_{pv} as a function of the external magnetic field magnitude $\mu_0 H$ applied at $\alpha = 10^\circ$ for $1.548 \text{ GHz} \leq \nu \leq 5.948 \text{ GHz}$. The measured dc photovoltage V_{pv} is displayed in Fig. 7 for selected rf frequencies. At the highest rf frequency $\nu = 5.948 \text{ GHz}$, two dominantly antisymmetric Lorentzian lines are observed at $\pm 37 \text{ mT}$. These lines shift to smaller magnitudes of

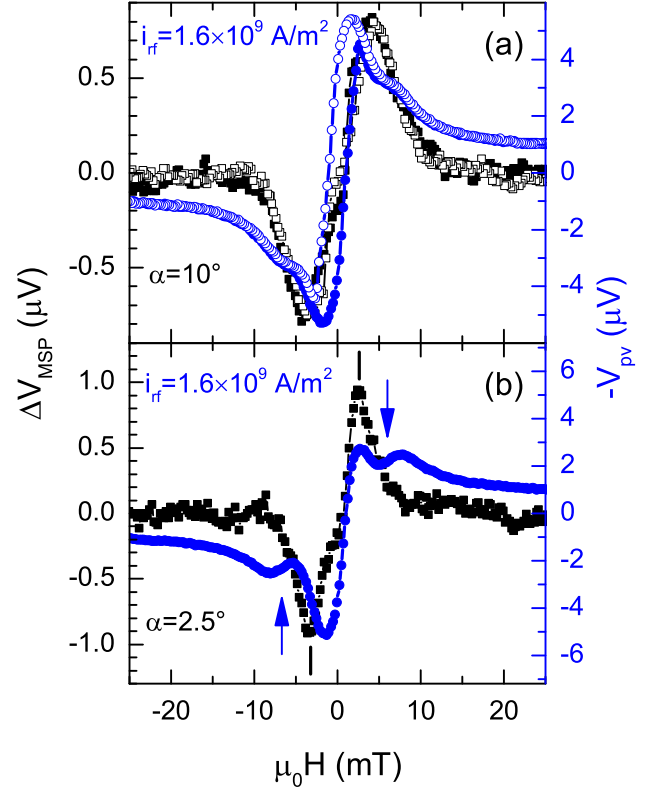


FIG. 8. (a) Comparison of ΔV_{MSP} and $-V_{pv}$ for $\alpha = 10^\circ$. The extrema in ΔV_{MSP} and V_{pv} are located at different values of $\mu_0 H$. Furthermore the respective lineshapes are different. This shows that ΔV_{MSP} and V_{pv} have different physical origins. (b) Comparison of ΔV_{MSP} and $-V_{pv}$ for $\alpha = 2.5^\circ$. The inflection point in V_{pv} corresponds to the FMR magnetic field (Kittel mode, indicated by the arrows). The extrema in ΔV_{MSP} (indicated by the vertical lines) are however shifted from the FMR magnetic field due to the characteristic angular dependence of the magnetoelastic driving field (see text).

the external magnetic field with decreasing rf frequency. Following Ref.³², we attribute these lines to the mixing signal caused by the torques due to the Oersted field of the rf current in the Pt layer and the spin transfer torque due to the spin current caused by the spin Hall effect. Furthermore, as particularly evident at lower frequencies, a hysteretic contribution to V_{pv} is observed around zero external magnetic field. This contribution is dominant at $\nu = 1.548 \text{ GHz}$ and is attributed to nonresonant spin rectification³¹. The dc voltage V_{pv} along the bilayer was proportional to the square of the rf current density in accordance to expectations^{28,32}.

Appendix C: Comparison to acoustic spin pumping

We now compare the dc photovoltage V_{pv} experimentally observed with $\mathbf{I}_{rf} \parallel \mathbf{y}$ to the measured inverse spin Hall voltage ΔV_{MSP} due to elastic spin pumping (see

main text). Fig. 8(a) shows ΔV_{MSP} (left scale, squares) and $-V_{\text{pv}}$ (right scale, circles), both determined with an rf frequency $\nu = 1.548$ GHz and the external magnetic field applied at $\alpha = 10^\circ$. The extrema in V_{pv} and ΔV_{MSP} are located at different values of $\mu_0 H$. Furthermore, the lineshapes are different, which in particular results in a finite V_{pv} at $|\mu_0 H| \geq 10$ mT, where ΔV_{MSP} vanishes. V_{pv} shows a dominant hysteretic feature around zero external magnetic field while hysteresis in ΔV_{MSP} is minimal. This clearly shows that ΔV_{MSP} and V_{pv} have different physical origins.

We moreover note that the extrema in the acoustic FMR signal ΔP_{SAW} (cf. Fig. 4(c) in the main text) do not necessarily coincide with the conventional ferromagnetic resonance field since the magnetoelastic driving field characteristically depends on \mathbf{M} orientation²⁴. As experimentally observed (cf. Fig. 4(c) in the main text), the extrema of ΔV_{MSP} and ΔP_{SAW} coincide - as expected for acoustic spin pumping. However, the extrema in ΔV_{MSP} are not necessarily located at the conventional FMR magnetic field observed in V_{pv} . This is particularly evident from Fig. 8(b), where we show ΔV_{MSP} and V_{pv} recorded with $\alpha = 2.5^\circ$ (only magnetic field upswing shown). The FMR field expected from the Kittel mode coincides with the inflection points in V_{pv} at approximately $\mu_0 H_{\text{res}} \approx \pm 7$ mT (marked by the arrows). The extrema in ΔV_{MSP} are however located at $\mu_0 H \approx \pm 3$ mT (marked by the vertical lines). This is expected for acoustically driven FMR, since in this case the absorbed power and thus the spin pumping signal is given by $V_{\text{MSP}} \propto P \propto h_{\text{ME}}^2 \chi^2$ ²⁴, where χ is the susceptibility and h_{ME} the magnetoelastic driving field. Depending on the anisotropy of the ferromagnet, the magnitude of h_{ME} depends on \mathbf{H} , in particular for low external magnetic fields. Therefore, the product $h_{\text{ME}}^2 \chi^2$ is not necessarily maximized at the extrema of χ . This is the reason for the apparent discrepancy between FMR field and ΔV_{MSP} extrema visible in Fig. 8(b). This furthermore proves that V_{MSP} is *not* caused by any rectification ef-

fects in the bilayer, as these would occur exactly at the conventional ferromagnetic resonance field.

In conclusion, the experiments with deliberately applied rf currents \mathbf{I}_{rf} show that V_{MSP} is not caused by microwave rectification of \mathbf{I}_{rf} induced by the surface acoustic wave. For $\mathbf{I}_{\text{rf}} \parallel \mathbf{x}$, rectification effects can not be the origin of V_{MSP} due to their different dependency on the orientation of \mathbf{H} . For $\mathbf{I}_{\text{rf}} \parallel \mathbf{y}$, we experimentally demonstrated that the resulting rectification voltage V_{pv} has a distinctly different lineshape than V_{MSP} . Again, rectification effects due to $\mathbf{I}_{\text{rf}} \parallel \mathbf{y}$ thus can not account for V_{MSP} observed.

Reversing this argument, we have experimentally shown that rf currents in the bilayer indeed give rise to rectification voltages at the conventional FMR field. The absence of a corresponding signal in V_{MSP} indicates that SAW-induced currents in the Co/Pt bilayer can safely be neglected in the interpretation of V_{MSP} .

Appendix D: Estimation of SAW-induced strain

Using vector network analysis, we determined the reflection parameter S_{11} of the input IDT as a function of frequency at zero external magnetic field. At the IDT operation frequency $\nu = 1.548$ GHz, we recorded $|S_{11}(\nu)|^2 = 0.16$, while outside the SAW passband frequency we found $|S_{11}(\nu \pm 4 \text{ MHz})|^2 = 0.20$. With $\Delta|S_{11}|^2 = 0.04$, we find $P_{\text{el}} = \Delta|S_{11}|^2 P_{\text{rf}} = 40$ mW for the electrical power and $P_{\text{acoustic}} = k^2 P_{\text{el}} = 2$ mW for the acoustic power with the LiNbO₃ coupling coefficient $k^2 = 5\%$ ³⁶. Due to the bidirectionality of the input IDT, the SAW traveling towards the bilayer carries only half of this power. With the acoustic wavelength $\lambda = 2.2$ μm and the IDT aperture $W = 500$ μm , $P_{\text{acoustic}} = 1$ mW results in a pure strain $\varepsilon = 9.8 \times 10^{-6}$ along \mathbf{x} ³⁹, as the lattice displacement along the SAW propagation typically is about 60% of the displacement along the surface normal³⁹.

* goennenwein@wmi.badw.de

- ¹ P. Sharma, *Science* **307**, 531 (2005).
- ² S. Takahashi and S. Maekawa, *Sci. Tech. Adv. Mater.* **9**, 014105 (2008).
- ³ K. Ando *et al.*, *J. Appl. Phys.* **109**, 103913 (2011).
- ⁴ Y. K. Kato *et al.*, *Science* **306**, 1910 (2004).
- ⁵ V. Sih *et al.*, *Phys. Rev. Lett.* **97**, 096605 (2006).
- ⁶ Y. Kajiura *et al.*, *Nature* **464**, 262 (2010).
- ⁷ K. Uchida *et al.*, *Nature* **455**, 778 (2008).
- ⁸ K. Uchida *et al.*, *Nat. Mater.* **9**, 894 (2010).
- ⁹ C. M. Jaworski *et al.*, *Nat. Mater.* **9**, 898 (2010).
- ¹⁰ C. M. Jaworski *et al.*, *Phys. Rev. Lett.* **106**, 186601 (2011).
- ¹¹ R. Urban, G. Woltersdorf, and B. Heinrich, *Phys. Rev. Lett.* **87**, 217204 (2001).
- ¹² Y. Tserkovnyak, A. Brataas, and G. E. W. Bauer, *Phys. Rev. Lett.* **88**, 117601 (2002).
- ¹³ Y. Tserkovnyak, A. Brataas, and G. E. W. Bauer, *Phys. Rev. B* **66**, 224403 (2002).
- ¹⁴ M. V. Costache *et al.*, *Phys. Rev. Lett.* **97**, 216603 (2006).
- ¹⁵ F. D. Czeschka *et al.*, *Phys. Rev. Lett.* **107**, 046601 (2011).
- ¹⁶ B. Heinrich *et al.*, *Phys. Rev. Lett.* **107**, 066604 (2011).
- ¹⁷ In spin Seebeck experiments, the investigation of the phonon-magnon interaction was limited to the application of temperature gradients and thus the non-resonant coupling of phonons and magnons.
- ¹⁸ K. Uchida *et al.*, *Nat Mater* **10**, 737 (2011).
- ¹⁹ H. Y. Inoue *et al.*, *J. Appl. Phys.* **102**, 083915 (2007).
- ²⁰ Y. S. Gui *et al.*, *Phys. Rev. Lett.* **98**, 107602 (2007).
- ²¹ O. Mosendz *et al.*, *Phys. Rev. Lett.* **104**, 046601 (2010).
- ²² J. E. Hirsch, *Phys. Rev. Lett.* **83**, 1834 (1999).
- ²³ E. Saitoh *et al.*, *Appl. Phys. Lett.* **88**, 182509 (2006).
- ²⁴ M. Weiler *et al.*, *Phys. Rev. Lett.* **106**, 117601 (2011).

- ²⁵ S. Chikazumi, *Physics of Ferromagnetism*, The international series of monographs on physics (Oxford Science Publications, New York, 1997), 2nd ed.
- ²⁶ S. Datta, *Surface Acoustic Wave Devices* (Prentice Hall, Englewood Cliffs, 1986).
- ²⁷ The SAW is a Rayleigh wave and thus has a finite transversal (shear) strain component as well. We neglect this component for simplicity.
- ²⁸ A. Yamaguchi *et al.*, Appl. Phys. Lett. **90**, 182507 (2007).
- ²⁹ L. H. Bai *et al.*, Applied Physics Letters **92**, 032504 (2008).
- ³⁰ See Supplemental Material at [URL will be inserted by publisher] for details.
- ³¹ X. F. Zhu *et al.*, Phys. Rev. B **83**, 140402 (2011).
- ³² L. Liu *et al.*, Phys. Rev. Lett. **106**, 036601 (2011).
- ³³ R was determined by a 2 point measurement and takes into account that only a fraction of the Co/Pt thin film bilayer is perturbed by the SAW.
- ³⁴ T. Gutjahr-Löser, D. Sander, and J. Kirschner, J. Magn. Magn. Mater. **220**, 1 (2000).
- ³⁵ M. Nishikawa *et al.*, J. Magn. Magn. Mater. **126**, 303 (1993).
- ³⁶ C. Campbell, *Surface Acoustic Wave Devices and Their Signal Processing Applications* (Academic Press, San Diego, 1989), 1st ed.
- ³⁷ T. R. McGuire and R. I. Potter, IEEE Trans. Magn. **11**, 1018 (1975).
- ³⁸ J. M. D. Coey, *Magnetism and Magnetic Materials* (Cambridge University Press, Cambridge, 2010), 1st ed.
- ³⁹ W. Robbins, IEEE T. Son. Ultrason. **24**, 339 (1977).